

Dual-Phosphorescent Heteroleptic Silver(I) Complex in Long-Lasting Red Light-Emitting Electrochemical Cells

Sophia Lipinski, Luca M. Cavinato, Thomas Pickl, Giulia Biffi, Alexander Pöthig, Pedro B. Coto,* Julio Fernández-Cestau,* and Rubén D. Costa*

The design of red-emitting silver(I) complexes and their implementation in thin-film lighting are still challenging as (i) their high ligand-field splitting energy leads to high-energy emissions with a controversial mechanism (thermally activated delayed fluorescence vs fluorescence/phosphorescence), and (ii) their low electrochemical stability leads to the formation of silver nanoclusters, limiting device stability to a few seconds. Herein, a thoughtful complex design [Ag(xantphos)(deebq)]PF₆ combining a large-bite angle diphosphine ligand (xantphos), a rigid, sterically hindered, π -extended biquinolin (deebq) is reported. In contrast to prior-art, this complex possesses (i) efficient red-emission ($\lambda_{em} = 660$ nm; photoluminescence quantum yield of 42%) assigned to a thermally equilibrated dual-phosphorescent emission based on spectroscopic/theoretical studies and (ii) stable reduction behavior without forming silver nanoclusters. This results in the first red light-emitting electrochemical cells featuring (i) improved stability of two orders of magnitude compared to prior-art (from seconds to hours) at irradiances of 20 $\mu\text{W cm}^{-2}$, and (ii) a new degradation mechanism exclusively related to p-doping as confirmed by electrochemical impedance spectroscopy analysis. Indeed, a multi-layered architecture to decouple hole injection/transport and exciton formation enables a further 2-fold enhanced irradiance/stability. Overall, this work illustrates that deciphering the rules for silver(I) complex design for lighting is tricky, but worthwhile.

1. Introduction

Light-emitting electrochemical cells (LECs) are the simplest and cheapest solid-state lighting (SSL) concept.^[1–5] They combine a single-layered architecture and air-stable electrodes with low-cost


and up-scalable solution-based fabrication techniques (spray- and dip-coating).^[6] Therefore, LECs are ideal for scalable smart- and soft-lighting applications, such as flexible/foldable labeling, medical, decoration, and signage purposes, among others.^[7,8] The success of the LEC concept lies in the nature of the active layer that consists of an electroluminescent compound blended with an ion-based electrolyte.^[9] Upon application of an external bias voltage, the beforehand randomly distributed mobile ions are polarized, creating electric double layers (EDLs) at the electrode interfaces.^[10,11] This allows efficient electron/hole injection from air-stable electrodes and the controlled growth of the p- and n-doped regions in a single active layer. The electron-hole recombination takes place in the resulting non-doped intrinsic region of the so-called p-i-n junction that features a dynamic behavior, changing in thickness and/or position over time.^[1–4,10,12]

Over the last two decades, a myriad of electroluminescent emitters,^[7,13–17] like conjugated polymers,^[18] small molecules,^[17,19] quantum dots,^[16,20] perovskites^[21] and ionic transition metal complexes (iTMCs)^[11,22,23] have been implemented in LECs. In particular, the performance of iTMCs-LECs with Ir(III) complexes stands out in terms of stabilities (>5000 h) and brightness (>500 cd m^{-2})^[24,25] for yellow and orange devices. However,

S. Lipinski, L. M. Cavinato, J. Fernández-Cestau, R. D. Costa
Technical University of Munich Campus Straubing
Chair of Biogenic Functional Materials
Schulgasse 22, 94315 Straubing, Germany
E-mail: julio.fernandez-cestau@tum.de; ruben.costa@tum.de

T. Pickl, A. Pöthig
TUM School of Natural Sciences, Department of Chemistry & Catalysis
Research Center (CRC)
Technical University of Munich
Lichtenbergstr. 4, 85747 Garching, Germany

G. Biffi, P. B. Coto
Materials Physics Center (CFM)
Spanish National Research Council (CSIC) and Donostia International
Physics Center (DIPC)
Paseo Manuel de Lardizabal 5, Donostia-San Sebastián 20018, Spain
E-mail: pedro.brana@csic.es

 The ORCID identification number(s) for the author(s) of this article can be found under <https://doi.org/10.1002/adom.202203145>

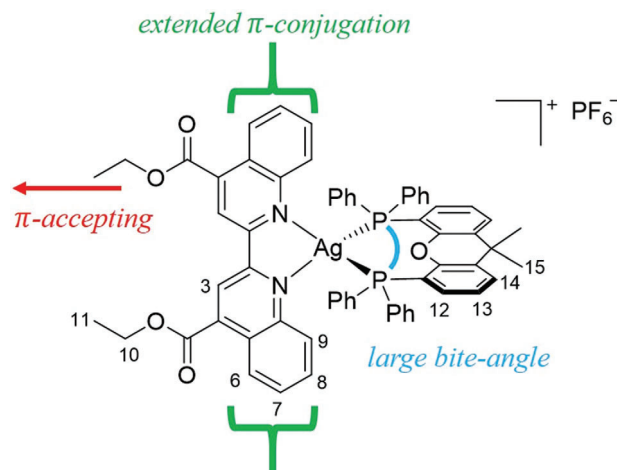
© 2023 The Authors. Advanced Optical Materials published by Wiley-VCH GmbH. This is an open access article under the terms of the Creative Commons Attribution-NonCommercial License, which permits use, distribution and reproduction in any medium, provided the original work is properly cited and is not used for commercial purposes.

DOI: 10.1002/adom.202203145

the presence of metal-centered excited states dramatically limits the performance of blue and green devices,^[26] while the costs associated with the scarcity of Ir (0.001 ppm in the Earth's crust) are not encouraging for large-area applications.^[27] Thus, more earth-abundant and cheaper iTMCs based on d¹⁰-complexes have been heralded to guide LECs into the market.^[13,14] On one hand, Cu(I)-iTMC-LECs have been exhaustively developed, spanning the whole visible range,^[22,28–33] including white.^[22,34–36] However, they exhibit major limitations, such as unforeseen changes in the emission features from crystalline powder to thin films and the prominent degradation – that is, oxidized species and penta-coordinated species – upon device fabrication and operation.^[37] In this context, Ag(I)-iTMCs have emerged as the most direct alternative getting the attention of the lighting community^[38–46] due to (i) high ligand field splitting energy, easily enabling the design of high-energy emitting complexes, (ii) high stability towards oxidation due to the high oxidation potential of Ag(I),^[47] and (iii) high photoluminescence quantum yields (PLQYs) associated to a controversial fluorescence, thermally activated delayed fluorescence (TADF), and/or phosphorescence mechanisms.^[42–46,48] To date, yellowish green LECs have been reported with mononuclear [Ag(bpy)(P[∗]P)]BF₄ – bpy refers to derivatives of 2,2'-bipyridine and P[∗]P has been POP (bis((2-diphenylphosphino) phenylether) and xantphos (4,5-bis((diphenylphosphino)-9,9-dimethylxanthene)^[38,40,41] – and trinuclear Ru(II)-Ag(I) complexes.^[48] These devices featured moderate efficiencies (< 1 cd A⁻¹) and poor stabilities (< 30 s) due to the formation of silver nanoclusters upon operation. The latter was circumvented using a multi-layered architecture with an electron transport layer, increasing the stability by 2 orders of magnitude. However, this strategy also modified the emission mechanism to an undesired exciplex-like broad emission spectrum, compromising the chromaticity of the device.^[41]

In light of the aforementioned, electrochemically stable and highly efficient Ag(I)-iTMCs spanning the whole visible range are paramount to set in their prospect in LECs. In particular, the design of low-energy emitting Ag(I)-iTMCs is challenging due to the low-energy lying d-orbitals,^[47] but crucial for white-emitting devices and NIR applications like bio-imaging or -sensing. Indeed, a handful of neutral/cationic low-energy emitting Ag(I) complexes have been reported. Teng et al. recently introduced an orange [Ag(N[∗]N)(P[∗]P)]⁺ complex (λ_{em} = 573 nm, PLQY of 62% in powder) bearing a donor-acceptor pyridine-substituted 1-phenyl-1H-phenanthro[9,10-d]imidazole framework modified with a 10H-phenoxazine (PXZ) as N[∗]N and POP as P[∗]P ligand.^[44] Here, the intrinsic TADF emission mechanism of PXZ was enhanced by the Ag(I) coordination, reducing the singlet-triplet energy splitting. In addition, the related orange organic light-emitting diodes featured slightly higher external quantum efficiencies (EQEs) than those based on analogous Cu(I) complexes. Further neutral dinuclear Ag(I) complexes,^[48,49] such as [Ag(dppcc)Cl]₂ (dppcc = *o*-bis(diphenyl-phosphino)-*o*-carborane), exhibited a red emission band (λ_{em} = 640 nm and PLQY of 6% in thin-film) that was attributed to a pure phosphorescence mechanism.^[48]

Herein, we rationalize the design of a red-emitting Ag(I)-iTMC combining a rigid, sterically hindered, and π-extended biquinolin (deebq = 4,4'-diethylester-2,2'-biquinoline) and xantphos ligands, leading to the complex [Ag(xantphos)(deebq)]PF₆ **1** – Scheme 1. This exhibited a remarkable red-emission (λ_{em}



Scheme 1. Chemical structure representation of [Ag(xantphos)(deebq)]PF₆ **1** including its design strategy.

= 660 nm and PLQY of 42% and 25% in thin-film and powder, respectively). This emission is attributed to a thermally equilibrated dual-phosphorescence – triplet-triplet energy splitting ($\Delta E_{T1A-T1B}$) of ≈ 0.05 eV for both powder and thin-film – between two mainly ligand-to-ligand charge transfer triplet excited states, as supported by theoretical studies based on density functional theory (DFT). In contrast to the prior-art, electrochemical assays in solution and electrochemical impedance spectroscopy in devices attested to the success of the complex design to prevent the formation of silver nanoclusters, however revealing an irreversible oxidation wave. Indeed, the unique photoluminescence and electrochemical features of **1** resulted in the first red-emitting Ag(I)-iTMC LECs (λ_{em} = 645 nm; x/γ Commission Internationale de l'Éclairage (CIE) color coordinates of 0.60/0.38) with outstanding performance compared to previous works.^[38,41,48] Specifically, pristine 1-LECs featured two orders of magnitude enhanced stabilities going from a few seconds to hours at moderate irradiance of 20 μW cm⁻² while decoupling hole injection/transport from exciton formation using a multi-layered device architecture as applied in Cu(I)-iTMC-LECs^[22,32,34,50] led to a 2-fold enhanced irradiance and stability.

All-in-all, this work provides a successful design of a red-emitting [Ag(N[∗]N)(P[∗]P)]⁺ complex with singular emission and electrochemical behaviors, representing a nice example that illustrates the complexity of designing emissive Ag(I)-iTMCs towards highly performing lighting devices.

2. Results and Discussion

2.1. Molecular Design, Synthesis, and Characterization

To prepare the red-emitting Ag(N[∗]N)(P[∗]P)]⁺ **1**, the commercially available xantphos ligand and the deebq were selected as P[∗]P and N[∗]N ligands, respectively. The choice of the deebq scaffold was motivated by its extended π-conjugation, while π-accepting ethyl ester/COOEt groups, characterized by a Hammett parameter of σ_p = 0.45,^[51] were attached to further reduce the energy level of the lowest unoccupied molecular orbital (LUMO) – vide infra. In addition, the biquinoline ligand can also be described as a

bipyridine ligand saturated at the 4,4', 5,5', and 6,6'-positions; a key feature to minimize geometrical distortions in analogous Cu(I)-iTMCs upon irradiation and electrochemical stress, leading to improved device performances.^[29–33,52] Finally, Nierengarten et al.^[53] and Housecroft and Constable et al.^[54] among others,^[55] have shown the benefits of combining large diphosphine bite-angles, such as xantphos, and a steric hindrance at the *ortho* position in bipyridine-based ligands to avoid the formation of low emissive homoleptic species during the synthesis, while they are also prone to evolve in solution under device fabrication conditions.^[40,41] In light of the aforementioned, we hypothesize that the combination of deebq and xantphos should avert the formation of (i) non-emissive homoleptic and penta-coordinated (Jahn–Teller distortion at the excited state) species during the synthesis and device fabrication and (ii) silver nanocluster upon electrochemical and irradiation stress.

First, deebq was prepared following a reported procedure.^[56] The synthesis of [Ag(xantphos)(deebq)]PF₆ **1** (Scheme 1) consists of mixing an equimolar amount of AgPF₆ and deebq in dichloromethane/CH₂Cl₂ followed by the addition of 1 eq. of xantphos under gentle stirring at room temperature, leading to an instantaneous color change from yellow to deep orange. This suggests the successful formation of **1** that is isolated as an orange powder in 80% yield – Experimental Section for more details. In contrast to the formation of homoleptic complexes in the synthesis of [Ag(bpy)(POP)]⁺ derivatives noted by Moudam and Fresta et al.,^[38,41] high-resolution mass spectrometry – ESI-MS; Figure S1, Supporting Information – and ¹H- and ³¹P{¹H}NMR spectroscopy – Figures S1–S3, Supporting Information – confirmed the exclusive formation of the desired heteroleptic species. Furthermore, ¹H- and ³¹P{¹H}NMR spectroscopy also attested that **1** is stable over long periods of time in relevant solvents for electrochemical assays (acetonitrile/CH₃CN) and device fabrication (tetrahydrofuran/THF) – Figures S4–S7, Supporting Information.

Slow diffusion of diethyl ether into a saturated solution of **1** in CH₂Cl₂ at room temperature and dark led to single crystals suitable for X-ray analysis. A representation of the molecular structure along with a selection of representative atomic distances and angles of **1** is summarized in Figure 1 and Table S1, Supporting Information. In short, the crystal structure confirms the heteroleptic nature of **1**, with both the xantphos and the deebq acting as chelating ligands. The τ_4 geometrical index for four-coordinated transition metal complexes defined by Houser et al.^[57] amounts to 0.84, suggesting a slightly less distorted tetrahedral geometry towards a trigonal pyramidal conformation compared to other [Ag(bpy)(P⁺P)]⁺ derivatives (0.7–0.8).^[38,41] Indeed, the N1–Ag–N2 (69.76(6)°) and P1–Ag–P2 (113.515(18)°) bite angles as well as N1–Ag and N2–Ag distances (2.3306(18) Å and 2.4553(17) Å) and P1–Ag and P2–Ag distances (2.4529(5) Å and 2.4753(6) Å) of **1** are comparable.^[38,40,41,58] Likewise, both quinoline moieties in deebq are twisted with the N1–C39–C48–N2 torsion angle of 16.7° in a similar fashion to reference compounds with bpy.^[38,40,41] Thus, the more ideal tetrahedral conformation must be driven by the extended π -conjugated system of the deebq that features a short π -intermolecular interaction between adjacent quinolines, with a centroid-centroid distance of 3.48 Å, and short C–H...F interactions (\approx 2.35–2.45 Å) involving the deebq and the PF₆ anion – Figure 1. The Lewis acidity of the aromatic

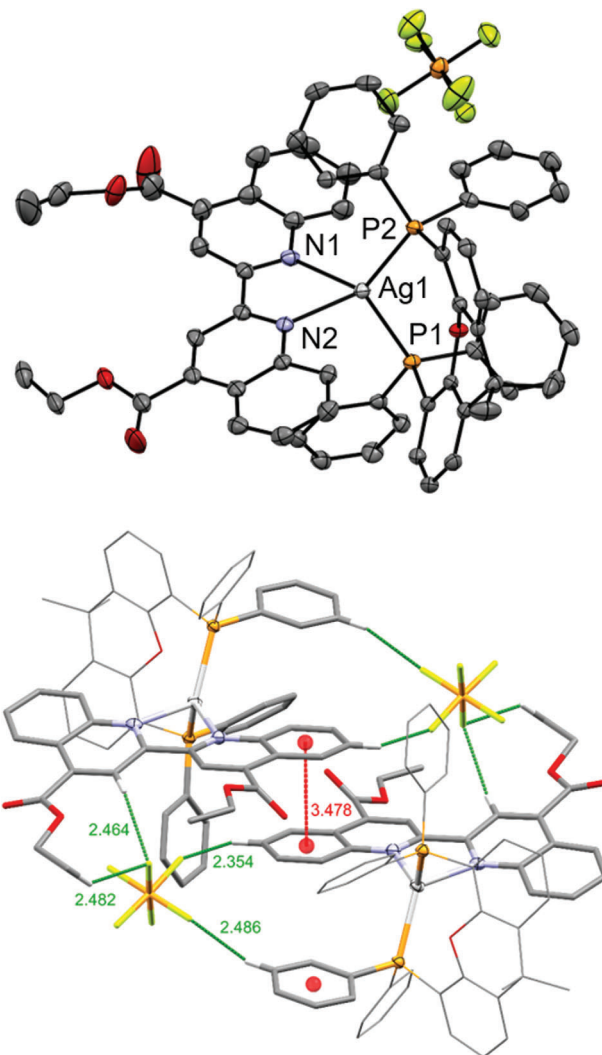


Figure 1. Top: X-ray structure of [Ag(xantphos)(deebq)]PF₆ · CH₂Cl₂. Solvent molecules, hydrogen atoms, and disorder in the COOEt groups are omitted for clarity. The atoms are represented as ellipsoids with a 50% probability level. Selected bond distances (Å) and angles (°): Ag1–P1 (2.4529(5)), Ag1–P2 (2.4753(6)), Ag1–N1 (2.3306(18)), Ag1–N2 (2.4553(17)), P1–Ag1–P2 (113.515(18)), N1–Ag1–N2 (69.76(6)), P2–Ag1–N1 (115.21(4)), and P1–Ag1–N2 (109.11(4)). Bottom: Extended molecular crystal packing of **1** revealing the presence of weak and strong intra- and intermolecular π -interactions as well as relatively strong C–H...F interactions between H-3 of deebq and a PF₆ anion.

hydrogen next to the COOEt substituent (named H-3 in Scheme 1) is, for example, further reflected in its unshielded position in the ¹H-NMR spectrum at 8.92 ppm – Figure S2, Supporting Information. Indeed, the intermolecular π -interactions are not present in the reference compounds,^[38,40,41] while strong C–H...F interactions might rule the molecular packing order. The introduction of substituents in the *ortho* position to the bpy has been established as a successful strategy to increase self-stability in heteroleptic Cu(I) complexes.^[29,30,52] Here, we propose an additional advantage of this strategy in analogous Ag(I) complexes. We hypothesize that the interaction of the *ortho*-to-the-nitrogen acidic proton with the anion in the solid state should be replaced by

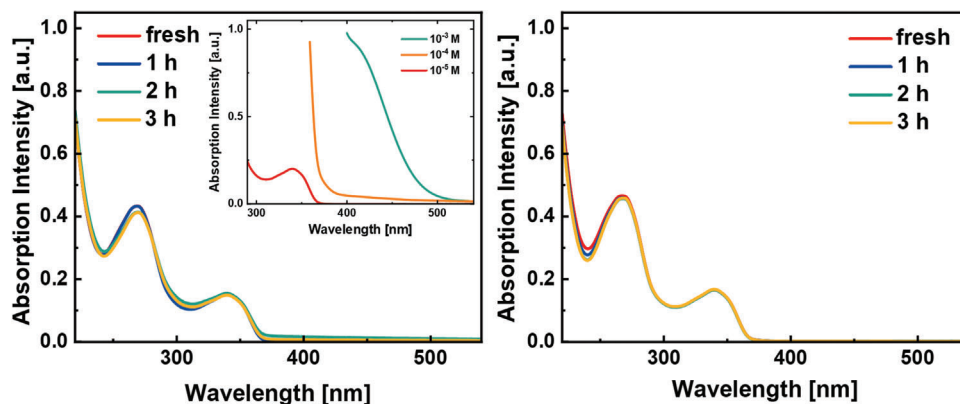


Figure 2. UV–vis absorption spectra of **1** (10^{-5} M) in THF under ambient/dark storage (left) and 1 sun per $70\text{ }^{\circ}\text{C}$ (right) over time. Inset: Zoom-in of the UV–vis absorption spectra at the low-energy region upon increasing concentration of **1** in THF – see the legend.

interaction with the solvent if basic solvents (CH_3CN or THF) are employed. The distortion of the bpy ligand caused by the accommodation of these interactions displays a plausible opening route towards the formation of silver nanoclusters in solution – vide infra.^[41,48]

2.2. Stability Behavior in Solution

$[\text{Ag}(\text{N}^{\wedge}\text{N})(\text{P}^{\wedge}\text{P})^+$ complexes are notorious for their low stability under irradiation and thermal stress as well as storage in solution even under ambient/dark conditions.^[41,59] These aspects are key to optimizing the performance of LECs as the fabrication steps include solvent-based thin-film deposition techniques and thermal treatments. Finally, device operation conditions also involve heat generation depending on the driving modes.^[60]

The stability of **1** in solution (THF and CH_3CN) under different conditions, that is, storage in the dark and combination of 1 sun irradiation (100 mW cm^{-2}) and thermal stress ($70\text{ }^{\circ}\text{C}$), was studied over time via UV–vis absorption and NMR techniques. Feasible processes that are prone to take place are (i) the formation of homoleptic species – Section 2.1, (ii) solvent-assisted ligand exchange due to the solvent coordination ability – that is, CH_3CN for electrochemical studies – Section 2.3, and THF for LEC fabrication – Section 2.5, and (iii) the formation of silver nanoclusters – Section 2.3.^[41,59] At first, the excellent storage stability was confirmed by the lack of changes in ^1H - and $^{31}\text{P}\{^1\text{H}\}$ NMR spectra over time up to 20 h – Figures S4–S7, Supporting Information. This is also confirmed by the absence of changes in the UV–vis absorption spectrum of **1** regardless of the above stress scenarios – **Figure 2**. The absorption features consist of two well-defined bands centered at 270 and 340 nm – **Figure 2** and **Figure S8**, Supporting Information, while the absorption spectra recorded in solvents of different polarities/dielectric constants reveal a charge transfer nature of the low-energy band – **Figure S8**, Supporting Information. Theoretical calculations using linear response time-dependent density functional theory (TDDFT) aided us in further characterizing the low-energy band of mixed nature combining excitations of metal-to-ligand (MLCT) charge transfer character and intra-ligand character. In detail, the analysis of the lowest-lying singlet excited states mainly con-

tributing to this band in terms of natural transition orbitals shows that in several of them, the excitation promotes an electron from an orbital exhibiting different degrees of localization on the Ag and P atoms to a π -like orbital localized on the deebq moiety. In addition to these states, there is also a significant contribution of intra-ligand (deebq) excitation character to the band – **Figure S10a**, Supporting Information. The high-energy features exhibit a more complex character merging contributions of different electronic excited states of different natures – **Table S3**, Supporting Information. In addition, upon increasing the concentration of **1**, a very low intense absorption band centered at 410 nm evolves – **Figure 2**. Based on our calculations, we assigned it to forbidden singlet-triplet electronic transitions caused by the small spin-orbit coupling interaction present in this system – **Table S4**, Supporting Information. Finally, the lack of absorption changes in the 325–375 nm range suggests the absence of silver nanoparticle formation.^[59]

Overall, **1** exhibits remarkable stability in solution allowing us to study its electrochemical features and to fabricate devices free of undesired degradative compounds. This strongly contrasts with the previous works on d^{10} complexes for lighting purposes.^[38,41,48]

2.3. Electrochemical Behavior in Solution

Cyclic voltammetry of **1** was performed in CH_3CN – **Table 1** and **Figure 3**. In short, irreversible oxidation at 1.88 V versus Fc/Fc^+ was noted. According to DFT calculations, the highest occupied molecular orbital (HOMO) is delocalized between the xantphos ligand and $\text{Ag}(\text{I})$ – **Figure 3**. The cathodic scan reveals two one-electron reduction processes at -1.41 and -1.78 V. They are assigned to the reduction of the $\text{N}^{\wedge}\text{N}$ ligand that defines predominantly the first LUMO levels – **Figure 3**. What is more relevant, the reversibility of both reductions was confirmed by (i) the ratio of the anodic and cathodic peak currents $i_{p,c}/i_{p,a}$ and (ii) the peak-to-peak separation ΔE – **Table 1**.^[61] The first reduction is quasi-reversible ($i_{p,c}/i_{p,a} = 0.82$, $\Delta E = 2.90\text{ mV}$), while the second reduction is almost ideally reversible ($i_{p,c}/i_{p,a} = 0.94$, $\Delta E = 58\text{ mV}$). As noted in the literature,^[41,48] upon the second cycle, an intense anodic peak located at -0.11 V typically dominates the electro-

Table 1. Photophysical properties of **1** in powder and in thin-film at 298 and 77 K and electrochemical features versus Fc/Fc^+ of **1** in $\text{CH}_3\text{CN}/\text{NBu}_4\text{PF}_6$ (0.1 M).

	Photoluminescence						Cyclic voltammetry						
	$\lambda_{\text{em}}/\lambda_{\text{exc}}$ [nm]	$\langle\tau\rangle/\lambda_{\text{em}}$ [μs]	ϕ [%]	$\langle k_r \rangle$ $\times 10^4$ [s^{-1}]	$\langle k_{\text{nr}} \rangle$ $\times 10^5$ [s^{-1}]	$\lambda_{\text{max}}/\lambda_{\text{exc}}$ [nm]	$\langle\tau\rangle/\lambda_{\text{em}}$ [μs]	ϕ [%]	$\langle k_r \rangle$ $\times 10^5$ [s^{-1}]	$\langle k_{\text{nr}} \rangle$ $\times 10^5$ [s^{-1}]	E_{ox} [V]/ E_{HOMO} [eV]	E_{red} [V]/ E_{LUMO} [eV]	ΔE (HOMO- LUMO) [eV]/[nm]
	Crystalline powder						Thin-film						
1, 298 K	658/480	2.26	24.6	8.13	2.49	655/450	2.38	41.8	1.76	2.45	1.88/ -6.19 ^{a)}	-1.41/ -1.78/ -3.55 ^{a)}	2.64/470
1, 77 K	550, 600, 650/362	3090/550 and 600, 561/650	25.8	-	-	555, 610, 660/362	2420/555 and 610, 595/660	69.6	-	-	-	-	-

^{a)} Calculated from oxidation/reduction potential of cyclic voltammetry.^[63]

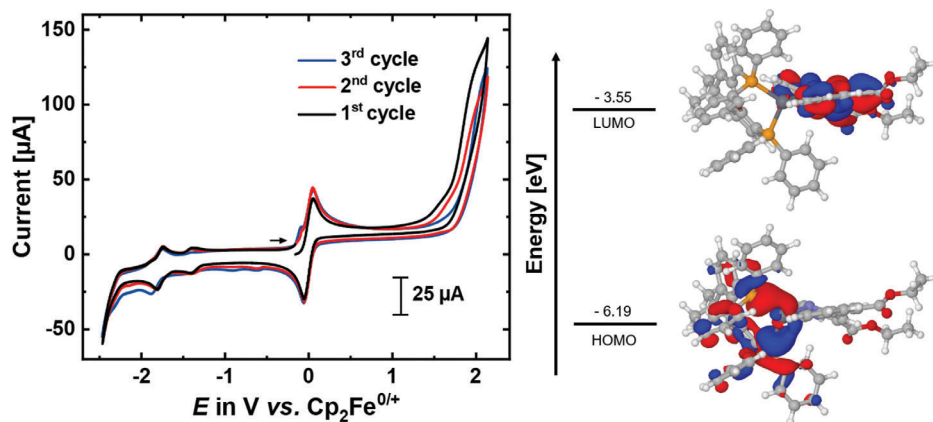


Figure 3. Left: Cyclic voltammogram of **1** (10^{-4} M; 100 mV s^{-1}) in $\text{CH}_3\text{CN}/\text{NBu}_4\text{PF}_6$ (0.1 M), at room temperature using (i) working electrode: platinum, (ii) counter electrode: platinum, and (iii) reference electrode: Ag/AgNO_3 . Right: HOMO and LUMO energies obtained from cyclic voltammetry and HOMO and LUMO representations of $[\text{Ag}(\text{xantphos})(\text{deebq})]^+$ calculated at the M062X/def2-TZVP level of theory.

chemical behavior of mononuclear and even heteronuclear $\text{Ag}(\text{I})$ complexes due to the formation of silver nanoclusters as the main degradation pathway. In sharp contrast, **1** displays no formation of silver nanoclusters during the second cycle, confirming the solution stability – vide supra. However, a degradation correlated to the irreversible oxidation process takes place – Figure 3. Thus, the hole injection/transport events in LECs should be considered as the limiting factor in terms of stability – Section 2.5, rather than the electron injection/transport events forming silver nanoclusters as reported by several authors.^[41,48] Indeed, the formation of silver nanoclusters was even barely noted during the third cycle, in which other degradation species are formed as the first reduction peak almost vanishes and the second reduction becomes partially irreversible – Figure 3.

2.4. Photoluminescence Behavior in Solid-State

The photoluminescence features of the crystalline powder and thin films (95 nm) were firstly characterized at 298 and 77 K. Thin films were prepared using the same procedure (spin-coating from a THF solution containing 20 mg mL^{-1} of **1**) and compo-

sition – that is, without the addition of other ionic electrolytes and/or polymer additives – to those used for LECs – Section 2.5. At first, atomic force microscopy (AFM) shows that the film exhibits a homogenous morphology without noticeable aggregates or phase separation with root-mean-square (RMS) values of 621 pm – Figure 4.

The emission spectra ($\lambda_{\text{exc}} = 480 \text{ nm}$) of both powder and thin film are characterized by the same featureless broad band with maxima at $\approx 660 \text{ nm}$ – Figure 4. While the excitation spectra of powder consist of an almost featureless broad band due to scattering events, thin films exhibit similar excitation spectra to that in solution – Figures 2 and 4. In addition, the PLQY in thin-film increased remarkably compared to that in powder (42% vs 25%; Table 1) caused by the loss of the supramolecular packing – Figure 1 – that typically favors self-quenching events. In line with this finding, the average excited state lifetimes ($\langle\tau\rangle$) in the thin film are slightly larger than those in powder – Table 1. Interestingly, the emission spectra drastically change at 77 K ($\lambda_{\text{exc}} = 362 \text{ nm}$), showing two additional well-resolved and intense peaks at ≈ 550 and 605 nm for both powder and thin films – Figure 4, which are all characterized by broad

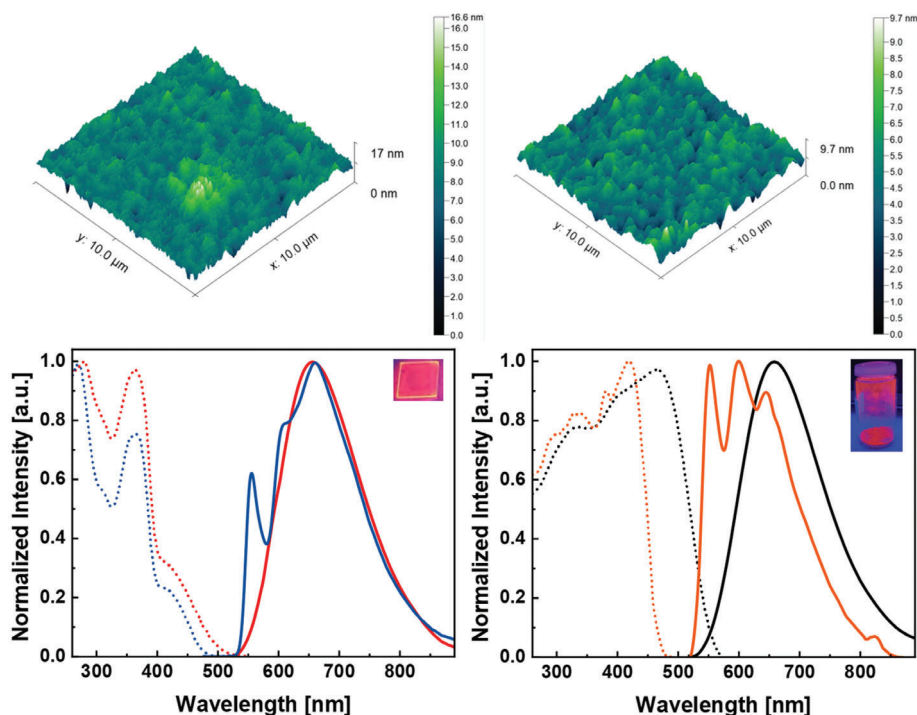


Figure 4. Top: AFM images of **1** (left) and **CBP-1-LECs** (ITO/PEDOT:PSS/CBP/1/Al, right) thin films. Bottom: Excitation (dotted line) and emission (solid line) spectra of **1** in thin-film (left) and powder (right) at 298 (red and black) and 77 K (blue and orange). Pictures of the thin films and the powder under UV irradiation ($\lambda_{\text{exc}} = 365 \text{ nm}$, 298 K) are shown as an inset.

emission-dependent excitation spectra – Figure S9, Supporting Information. This contrasts with what could be expected for a TADF d^{10} -complex,^[13,14] in which a red-shifted emission spectrum indicates the presence of an emissive triplet excited state – i.e., pure phosphorescence – that is in thermal equilibrium with the lowest-lying singlet excited state – i.e., delayed fluorescence. Though the new high-energy peaks could be related to a well-defined vibrational progression at 77 K, their τ values – i.e., 2.42 ms (thin-film) and 3.09 ms (powder) – Table 1 – are different from those of the low-energy peak at 660 nm – i.e., 595 μs (thin film) and 561 μs (powder) – Table 1. This suggests the existence of two triplet excited states (T_{1A} and T_{1B}) that are in thermal equilibrium – Figure 5. To support this claim, the changes in τ of the low-energy peak were monitored upon heating from 77 to 380 K. As shown in Figure 5, the τ versus T graph exhibits a sharp drop of τ upon heating, reaching a plateau at around 170 K when the population of the low-energy lying triplet (T_{1B}) state dominates. The lack of a plateau at 77 K indicates that the energy gap between both triplet excited states ($\Delta E_{T_{1A}-T_{1B}}$) is very small, maintaining their populations under thermal equilibrium. Indeed, an $\Delta E_{T_{1A}-T_{1B}}$ of $\approx 0.05 \text{ eV}$ for both thin film and powder was calculated, fitting this data with a two-state Boltzmann-type equation assuming a thermal equilibration between T_{1A} and T_{1B} – see Experimental Section for details.

To get insight into the nature of the excited states involved in the emission mechanism, the equilibrium structures of the lowest-lying triplet and singlet states of $[\text{Ag}(\text{xantphos})(\text{deebq})]^+$ were calculated using both, DFT and TDDFT methods – see Experimental Section and Supporting Information – Tables S4–S6. Our results indicate the existence of two low-lying triplet equilib-

rium structures, whose main structural difference is in one of the Ag-P distances, 2.729 and 3.168 Å for T_{1A} and T_{1B} , respectively – Figure 5. The nature of both triplet electronic states is similar and can be described in terms of natural transition orbitals as mainly involving ligand-to-ligand charge transfer (LLCT) transitions with minor MLCT in the case of T_{1B} . However, whereas T_{1A} can be characterized as an intra-ligand transition localized in the deebq moiety, T_{1B} exhibits an inter-ligand CT character from the xantphos to the deebq. – see Supporting Information. From an energetic point of view, these states exhibit a small energy difference ($E_{T_{1A}-T_{1B}} = 0.15/0.06 \text{ eV}$ with and without including the zero-point energy, respectively) in line with the experimental results. Finally, vertical energy differences ($T_{1A/B} \rightarrow S_0$, ΔE_{SCF}) of 2.09 eV (593 nm) and 1.71 eV (726 nm) were found for T_{1A} and T_{1B} , respectively – Tables S2 and S3, Supporting Information. These values are in line with the experimental findings, further supporting the assignment of the emission mechanism of **1** to a thermally equilibrated dual-phosphorescence. Though this behavior could at first sight be considered exotic, the presence of thermally stimulated and equilibrated phosphorescent processes in related Cu(I), Ag(I), and Au(III) complexes have been recently discussed.^[62]

2.5. Electroluminescent Behavior in Light-Emitting Electrochemical Cells

LECs were prepared by firstly spin-coating a 55 nm layer of poly(3,4-ethylene-dioxythiophene):polystyrene sulfonate (PEDOT:PSS) on a glass substrate coated with indium tin oxide (ITO)

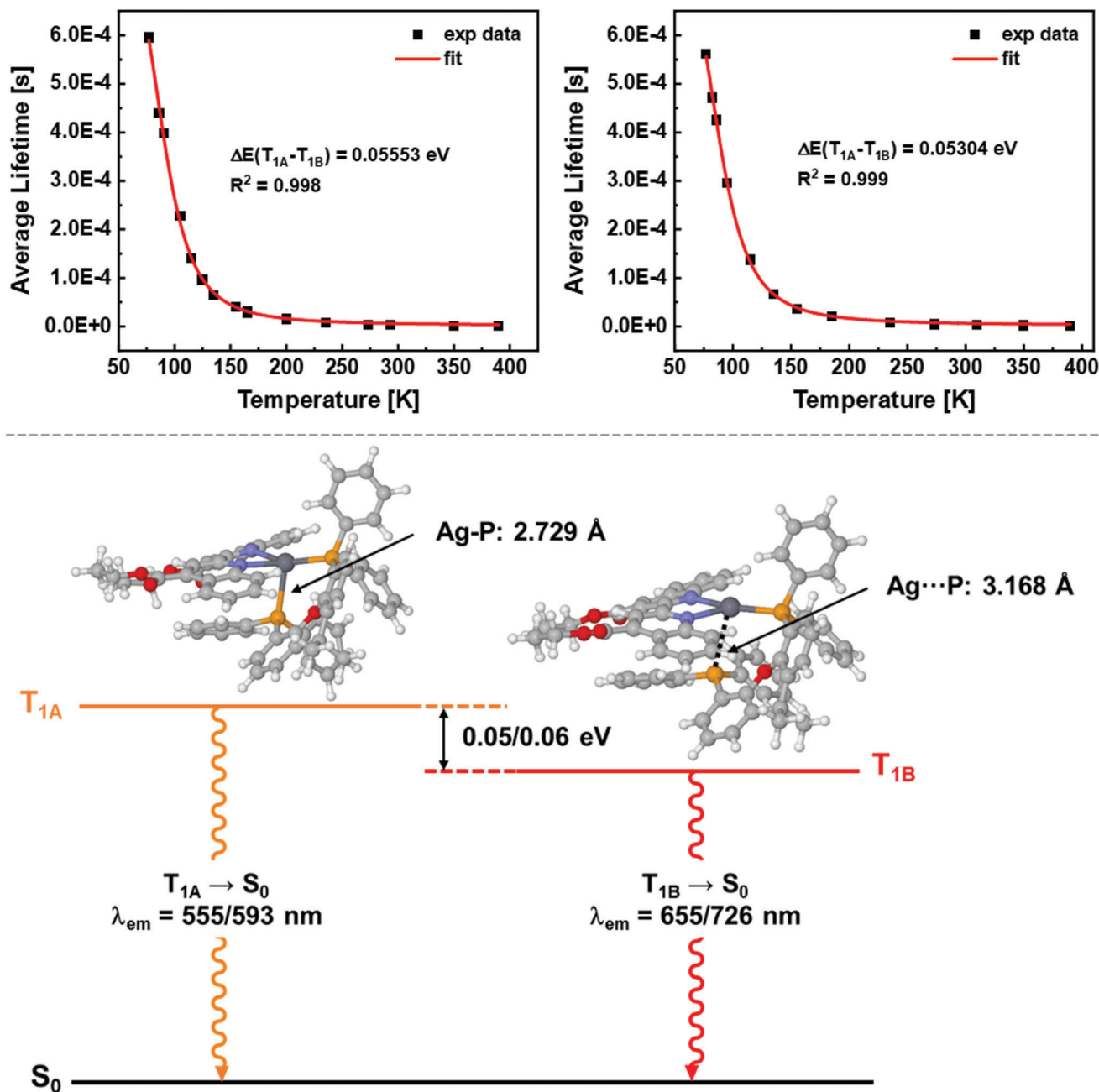


Figure 5. Top: τ versus T plots along the fitted equation (red) for thin-film (left) and crystalline powder (right). Bottom: Schematic representation of the involved triplet excited states of **1**, including geometry-optimized structures of T_{1A} and T_{1B} , the experimentally obtained/calculated values of the emission wavelengths and the energy gap to highlight the thermal equilibration situation.

to ensure reproducibility. This is followed by a layer of **1** (95 nm) spin-coated from a THF solution. Finally, the aluminum cathode (100 nm) was deposited onto **1** layer by physical vapor deposition – see Experimental Section for details.

The devices were driven at a pulsed current of 20 mA with a driving scheme based on a block wave at 1000 Hz and a duty cycle of 50%. The devices follow the typical LEC behavior with an instantaneous emission that rises, reaching irradiances (Irr_{max}) of $\approx 20 \mu W cm^{-2}$ or $6 cd m^{-2}$ and EQE of 3×10^{-3} %. This corresponds to a featureless broad emission band with a max-

imum at 645 nm associated with x/y CIE color coordinates of 0.60/0.38, corresponding to a red emission that is stable over the whole device operation – **Figure 6**. Compared to the photoluminescent emission spectrum of **1** in thin film – **Figure 4**, the electroluminescent emission is slightly blue-shifted (< 10 nm), which is consistent with polarization effects caused by the applied voltage – **Figure 6**.^[64] Thus, the energetically lowest-lying triplet state T_{1B} is also the emitting state under electric stimuli.

As the irradiance increases, the initial average voltage (3.7 V) decreases to a minimum value of 3.4 V – **Figure 6**. This is

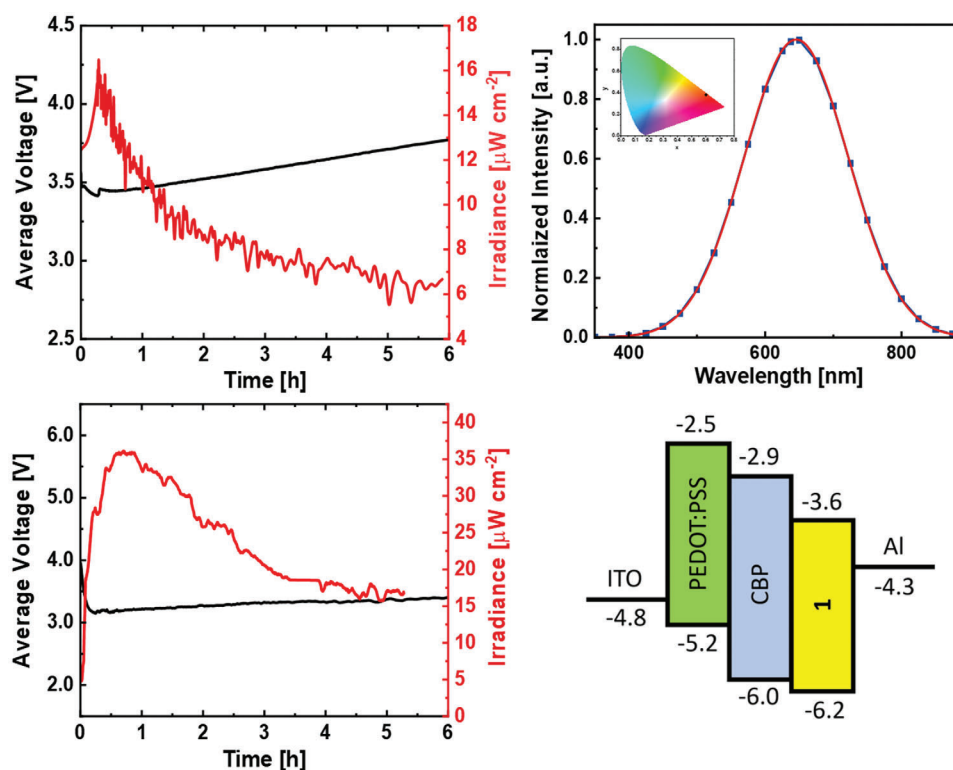


Figure 6. Top: Average voltage (black) and irradiance (red) versus time (left) and initial (red line) and half-life (blue squares) electroluminescence responses with the x/y CIE color coordinates as inset (right) of 1-LEC (ITO/PEDOT:PSS/1/Al) driven at pulsed 20 mA. Bottom: Average voltage (black) and irradiance (red) versus time (left) of CBP-1-LEC, driven at pulsed 20 mA (left) and schematic representation of the energy levels for the multi-layered device (right).

Table 2. Figures-of-merit and EIS parameters of 1-LECs and CBP-1-LECs.

Active layer	LEC			EIS			
	$I_{rr,max}^a$ [mW cm ⁻²]	$t_{1/2}^b$ [h]	λ_{max} (x/y CIE) [nm]	R_{LEC}^c [W]	σ^c [S m ⁻¹]	C_{eff}^c [nF]	ϵ_r^c
1	18.46	2.5	645 (0.60/0.38)	1.46×10^4	6.51×10^{-7}	0.591	0.634
				1.32×10^7	7.22×10^{-10}	46.1	49.5
CBP-1	36.39	5.0	645 (0.60/0.38)	2.20×10^5	4.04×10^{-8}	12.7	12.8
				3.83×10^5	2.32×10^{-8}	15.8	15.8

^{a)} Maximum irradiance achieved throughout the measurements; ^{b)} Time at which the maximum luminance halves its value; ^{c)} The top/bottom values refer to fresh/post-mortem devices.

attributed to the formation of the EDLs at the electrode interface that efficiently reduces charge injection barriers leading to ohmic contacts.^[1] However, a stable voltage plateau is not reached. Indeed, the voltage increases steadily, suggesting a severe electrochemical degradation that is indiscernible due to the lack of black spots or pin-holes – vide supra.^[24] This results in a strong reduction of the irradiance, reaching a device lifetime ($t_{1/2}$) of 2.5 h – Figure 6 and Table 2. Though the device stability is moderate compared to Cu(I)-iTMC-LECs,^[13,22,29–33,52] it represents 2-orders of magnitude enhancement compared to the prior-art Ag(I)-iTMCs-LECs that exhibited lifetimes of few seconds.^[38,41,48] In line with the electrochemical studies – Section 2.3, the stability enhancement is related to the absence of silver nanoclusters at the cathode interface that should have

led to a constant reduction of the applied voltage profile without forming a stable p-i-n junction.^[41]

To gain a deeper understanding of the degradation of 1-LECs, static electrochemical impedance spectroscopy (EIS) assays at voltages ranging from 0 to 4 V and frequencies from 1 to 1×10^6 Hz were conducted – Figure 7. EIS analyses of the Nyquist plots were performed using the equivalent circuit model as described in the Experimental Section and shown in Figures S11 and S12, Supporting Information. The typical LEC resistance profile shows two regimes. At applied biases below the energy band gap of the emitter, the resistance decreases exponentially. This is related to the formation of EDLs stemming from the polarization of the ions toward the electrode interfaces. At higher voltages, efficient charge injection takes place followed by the growth

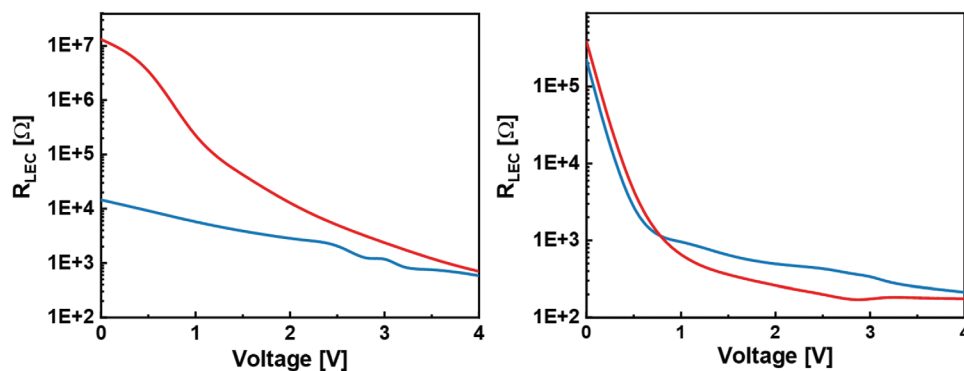


Figure 7. Changes in R_{LEC} of fresh (blue) and post-mortem (red) 1-LECs (left) and CBP-1-LECs (right) under static EIS measurements (0–4 V).

of the p- and n-doped regions.^[64,65] Simultaneously, the p-i-n region reduces, which is reflected by a change in the slope of the resistance profile owing to the ohmic contact.^[10,66] At 0 V, an ion conductivity (σ) of $6.15 \times 10^{-7} \Omega \text{ m}^{-1}$ and a dielectric constant (ϵ_r) of 6.34×10^{-1} were calculated – Figure 7, Table 2 and Experimental Section for details. In post-mortem devices, the resistance at 0 V increases three orders of magnitudes ($1.32 \times 10^7 \Omega$ vs $1.46 \times 10^4 \Omega$), leading to a significantly reduced ionic conductivity ($7.22 \times 10^{-10} \text{ S m}^{-1}$) – Table 2. Any formation of silver nanoclusters in the device would be reflected in a strong decrease in the resistance at 0 V of the post-mortem device.^[41] Thus, the direct comparison of the EIS resistance profile confirms the hypothesis of a detrimental oxidative degradation process as the main degradation mechanism – Section 2.3.

Following previous works on Cu(I)-iTMCs,^[32,34,35] a multi-layered LEC architecture to decouple hole injection/transport and exciton formation was applied to further optimize the device performance. Based on the calculated energy levels of the HOMO and the LUMO, 4,4'-bis(N-carbazolyl)-1,1'-biphenyl (CBP) was chosen as a suitable hole-transport material, resulting in the device architecture ITO/PEDOT:PSS/CBP(24 nm)/1/Al, CBP-1-LECs – Figure 6. The device was fabricated using the same procedure reported above – Experimental Section for details. AFM assays confirm that the morphology of the active layer 1 was not affected – Figure 4. The CBP-1-LECs were measured under the same conditions described above. As shown in the voltage and irradiance profile monitored over time, the device performance is greatly improved, reaching (i) irradiances of $\approx 40 \mu\text{W cm}^{-2}$, and (ii) lifetimes of 5 h as the voltage profile reduces to reach a plateau that holds over time, indicating that (i) the electrochemical degradation upon hole injection has been successfully alleviated and (ii) the enhanced hole injection rate might have change the position of the neutral emissive zone reducing the exciton quenching – Figures 6 and 7.^[1,35] Indeed, the EIS analysis confirms that the resistance at 0 V along with ionic conductivity and dielectric constants for the fresh and post-mortem devices are similar – Figure 7 and Table 2. The maximum irradiance level corresponds to a brightness of 12 cd m^{-2} and an EQE of $6 \times 10^{-3} \%$.

3. Conclusion

This work rationalizes a successful design for the first heteroleptic red-emitting Ag(I)-iTMC ($[\text{Ag}(\text{xantphos})(\text{deebq})]\text{PF}_6$) complex

combining (i) a π -extended biquinolin (deebq) unit featuring π -accepting ethyl ester groups to further reduce the LUMO level and a saturated *ortho* position to increase rigidity and steric hindrance and (ii) a large bite-angle xantphos ligand to exclusively form the heteroleptic species. The headlines of this design lie in three major aspects. In contrast to the prior-art, this complex exhibits an excellent self-stability in solution and under stress conditions (temperature/irradiation) as confirmed by UV-vis absorption, ESI-MS, and ^1H - and $^{31}\text{P}\{^1\text{H}\}$ -NMR spectroscopy and improved electrochemical stability upon reduction, showing the lack of silver nanoclusters formation that has been critical in the stability of thin-film lighting devices based on both mono-/di-nuclear Ag(I) complexes.^[38,41,48] In addition, an efficient red emission (660 nm, PLQY of 42% in thin-film) was attributed to a unique dual-phosphorescence mechanism (two thermally equilibrated triplet excited states with mostly intra-ligand and inter-ligand CT character, respectively) using temperature-dependent time-resolved emission spectroscopy and theoretical calculations. Overall, these assets led to the first red-emitting Ag(I)-iTMC-LEC that outperforms the prior-art stabilities going from seconds to hours (2 orders of magnitude) with enhanced irradiance. Here, ESI studies nicely confirmed the lack of silver nanoclusters formation, while a multi-layered device architecture to decouple hole injection/transport and exciton formation led to a further 2-fold enhanced irradiance and stability.

All-in-all, this work sets in a step-stone highlighting how the ligand design is key to ensure the great potential of Ag(I)-iTMCs as highly emissive and electrochemically stable alternatives to Cu(I)-iTMCs for thin-film lighting, in general, and LECs, in particular.

4. Experimental Section

Materials: All reactions were conducted under a dry nitrogen inert gas atmosphere using Schlenk or glovebox techniques. Solvents used for moisture- and air-sensitive reactions were obtained from the MBraun MB-SPS solvent purification system. All chemicals were purchased from chemical suppliers and used without further purification. 4,4'-diethylester-2,2'-biquinoline (deebq) was synthesized as reported in the literature.^[56]

Synthesis of $[\text{Ag}(\text{xantphos})(\text{deebq})]\text{PF}_6$: AgPF_6 (50.0 mg, 198 μmol , 1.0 eq.) and xantphos (114 mg, 198 μmol , 1.0 eq.) were dissolved in CH_2Cl_2 (30 mL) and stirred at room temperature for 20 min. Then, deebq (79.2 mg, 198 μmol , 1.0 eq.) was added causing a yellow, turbid solution. After stirring at room temperature for 10 min, the solution was

concentrated under vacuum (5 mL). The addition of hexane gave yellow crystals, which were washed with diethyl ether and dried under vacuum. Single crystals for X-ray diffraction were grown by slow diffusion of diethyl ether and hexane into a CH₂Cl₂ solution at room temperature. Yield: 195 mg (80%). ¹H-NMR (400 MHz, chloroform-*d*₁, δ): 8.92 (s, 2H, H-3), 8.76 (d, ³J_{HH} = 8, 2H, H-9), 8.00 (d, ³J_{HH} = 8, 2H, H-8), 7.76 (d, ³J_{HH} = 7, 2H, H-6), 7.67 (t, ³J_{HH} = 7, 2H, H-7), 7.37-6.53 (m, 24H, PPh₂, H-13, H-14), 6.55 (m, 2H, H-12), 4.64 (q, ³J_{HH} = 7, 4H, H-10), 1.84 (s, 6H, H-15), 1.56 (t, ³J_{HH} = 7, 6H, H-11). ³¹P{¹H}-NMR (162 MHz, chloroform-*d*₁, δ): -5.30 (dd, ¹J(³¹P-¹⁰⁷Ag) = 363 Hz, ¹J(³¹P-¹⁰⁹Ag) = 417 Hz), -144.6 (sept, PF₆). HRMS (ESI) *m/z*: [M + H]⁺ calc. for [C₆₃H₅₂O₅N₂AgP₂]⁺, 1085.23969; found, 1085.23932.

Theoretical Methods: The equilibrium structures of the ground state, T_{1A} and T_{1B} states were obtained using DFT.^[68] The M06-2X exchange-correlation potential^[69] and the def2-TZVP basis set^[70] were used. The core electrons of Ag were described using the def2-ECP pseudopotential.^[71] In addition, and to assess the possible role of thermally activated delayed fluorescence in this system, the equilibrium structures of the two lowest-lying singlet excited states S_{1A} and S_{1B} (see Supporting Information) were obtained using linear-response TDDFT^[72] and the same exchange-correlation functional and basis set. Solvent effects were incorporated by relaxing the structures of all the states mentioned above using the conductor-like polarizable continuum solvent model (CPCM)^[73] with tetrahydrofuran as solvent. State characterization was carried out by analyzing the largest single excitation contributions and constructing the natural transition orbitals for the different excited states.^[74] All these calculations were carried out using Gaussian 16.^[75] Spin-orbit coupling TDDFT calculations including 50 singlet and 50 triplet states were carried out at the ground state optimized structure of [Ag(xantphos)(deebq)]⁺, using the zero-order regular approximation (ZORA) Hamiltonian,^[76] the M06-2X exchange-correlation functional, and the ZORA recontracted def2-TZVP and SARC-ZORA-TZVP basis set for Ag.^[77] as implemented in ORCA 5.0.3. The corresponding Coulomb fitting auxiliary basis sets were used.^[78] The spin-orbit integrals were calculated using the RI-SOMF(1X) approximation.^[79]

Experimental Characterization Methods: X-ray crystallographic data were collected on a Bruker D8 Venture single crystal X-ray diffractometer equipped with a CPAD detector (Bruker Photon-II), an IMS microsource with MoK_α radiation (λ = 0.71073 Å), and a Helios optic, using the APEX4 software package. Measurements were performed on single crystals coated with perfluorinated ether. The crystals were fixed on top of a Kapton micro sampler and frozen under a stream of cold nitrogen. A matrix scan was used to determine the initial lattice parameters. Reflections were corrected for Lorentz and polarisation effects, scan speed, and background using SAINT. Absorption corrections including odd and even ordered spherical harmonics were performed using SADABS. Space group assignments were based upon systematic absences, E statistics, and successful refinement of the structures. The structures were solved using SHELXT with the aid of successive difference Fourier maps and were refined against all data using SHELXL in conjunction with SHELXLE.^[80,81] Hydrogen atoms were placed in calculated positions and refined using a riding model, with methylene, aromatic, and other C–H distances of 0.99, 0.95, and 1.00 Å, respectively, and U_{iso}(H) = 1.2•U_{eq}(C). Non-hydrogen atoms were refined with anisotropic displacement parameters. Full-matrix least-squares refinements were performed by minimizing Σw(F_o² – F_c²)² with the SHELXL weighting scheme.^[81] One of the ethyl ester functionalities attached to the deebq backbone was heavily disordered over three positions and was modeled by using free variables (SUMP) and by applying rigorous SIMU, RIGU, and SADI restraints. Disordered dichloromethane was treated similarly. Neutral atom scattering factors for all atoms and anomalous dispersion corrections for the non-hydrogen atoms were taken from “International Tables for Crystallography”.^[82] Images of the crystal structures were generated with Mercury. CCDC number 2232405 contains the supplementary crystallographic data for [Ag(xantphos)(deebq)]PF₆ (1). These data are provided free of charge by the joint Structures service of Cambridge Crystallographic Data Centre and Fachinformationszentrum Karlsruhe Access (www.ccdc.cam.ac.uk/structures).

Liquid-chromatography coupled with high-resolution mass spectrometry (HPLC-HRMS) was performed in positive mode using a Thermo Fisher Ultimate3000 with Scientific Vanquish Flex UHPLC and a Thermo Fisher Orbitrap (Exactive Plus with Extend Mass Range: Source HESI II). The detector was a Vanquish PDA Detector (VF-XX, detection ≤ 5 ppm). The reverse phase column was a Thermo Fisher Acclaim Phenyl 1, (column size: 2.1 × 150 mm, particles size: 3 μm). ¹H, ³¹P spectra were recorded on a JEOL JNM ECA 400 MHz spectrometer (Jeol, Freising, Germany). Chemical shifts are reported in ppm relative to tetramethylsilane and calibrated to the residual of the used deuterated solvents as an internal standard for the ¹H NMR. MestReNova software by Mestrelab Research S.L. was used for data evaluation. Absorption spectra were measured with a Shimadzu UV-2600i UV–vis Spectrophotometer. Photoluminescence spectra were recorded with an FS5 spectrofluorometer at 25 °C, and PLQY values were also measured at the same temperature with the FS5 spectrofluorometer using the integrating sphere SC-30 (Edinburgh Instruments). Photoluminescence measurements of 1 at temperatures ranging from 77 to 400 K were conducted in powder and thin film in Optistat-DN (Oxford Instruments) equipped with a temperature controller. Excited state decay lifetimes (τ) were measured with a microsecond flashlamp (λ_{exc} = 480 nm, 10 Hz and λ_{exc} = 362 nm, 10 Hz). The photoluminescence spectra were recorded after 5 min of equilibrating the temperature of the sample to ensure complete sample thermalization. The following equation was applied to calculate the average lifetime.

$$\langle \tau \rangle = \frac{\sum_i A_i \tau_i^2}{\sum_i A_i \tau_i} \quad (1)$$

The energy splitting between T_{1A} and T_{1B} was estimated with the following Boltzmann-type equation:

$$\langle \tau \rangle = \frac{1 + \exp\left(\frac{-\Delta E_{T_{1A}-T_{1B}}}{k_B T}\right)}{\frac{1}{\tau(T_{1B})} + \frac{1}{\tau(T_{1A})} \exp\left(\frac{-\Delta E_{T_{1A}-T_{1B}}}{k_B T}\right)} \quad (2)$$

while k_B is the Boltzmann constant and τ(T_{1B}) and τ(T_{1A}) corresponds to the decay times of T_{1A} and T_{1B}. Cyclic voltammetry measurements were carried out in a cylindrical one-compartment cell with a three-electrode set-up. A platinum disk working electrode with a diameter of 3.0 mm, a Pt wire as counter, and Ag/Ag⁺ wire as reference electrodes were used. Prior to every measurement, the working electrode was polished with alumina slurry 0.04 mm from Schmitz Metallographie GmbH. The potential was controlled by a Metrohm μAutolab III potentiostat. All measurements were conducted at 100 mV s⁻¹ under an inert nitrogen atmosphere with dry and degassed acetonitrile containing 0.1 M tetrabutylammonium hexafluorophosphate as a supporting electrolyte. Ferrocene was added as an internal standard to reference the acquired data to Fc⁺¹⁰. A filtered solution of 1 (20 mg mL⁻¹ in THF) was spin-coated at 2500 rpm for 60 s to give thin films, whose topography images were then obtained with a MFP-3D Origin+ AFM (Asylum Research) and elaborated with Gwyddion evaluation software.

Device Fabrication and Characterization Methods: Indium-tin oxide (ITO) substrates were purchased from Naranjo Substrates with an ITO thickness of 130 nm. Prior to use, they were extensively cleaned using detergent, water, ethanol, and propan-2-ol as solvents in an ultrasonic bath (frequency 37–70 Hz) for 15 min each, followed by drying the slides with N₂ gas and then treated with a UV-ozone cleaner for 8 min. The clean plates were coated with 55 nm PEDOT:PSS layers using the spin-coating technique. To this end, an aqueous solution of PEDOT:PSS was filtered and mixed with propan-2-ol in a ratio of 3:1. From this solution 50 μL were dropped onto the substrate at a rotation speed of 2000 rpm and spin for 60 s. The resulting layers were dried on a hotplate at 120 °C. A solution of 1 (20 mg mL⁻¹) was spin-coated on top of the PEDOT:PSS layer at 2500 rpm for 60 s and at 3000 rpm for an additional 10 s resulting in 95–100 nm thick films. Prior to the spin-coating process, the solutions were filtered with a 0.2 mm PTFE syringe filter. For the multi-layered devices, the THF solution of CBP (2 mg mL⁻¹) was spin-coated on top of the PEDOT:PSS layer

before complex 1 at 3000 rpm for 60 s, yielding thicknesses of 24 nm. In all cases, after the deposition of the active layer, the devices were transferred to an inert atmosphere glovebox (< 0.1 ppm O_2 and H_2O , Angstrom Engineering). Onto all devices, an aluminum cathode electrode (90 nm) was thermally evaporated using a shadow mask under high vacuum ($< 1 \times 10^{-6}$ mbar) in an Angstrom Covap evaporator integrated into the inert atmosphere glovebox. The device statistics involved up to five different devices – that is, a total number of 20 pixels. Time dependence of luminance, voltage, and current was measured by applying constant and/or pulsed voltage and current by monitoring the desired parameters simultaneously using an Avantes spectrophotometer (Avaspec-ULS2048L-USB2) in conjunction with a calibrated integrated sphere Avasphere 30-Irrad and Botest OLT OLED Lifetime-Test System. Electroluminescence spectra were recorded using the above-mentioned spectrophotometer. EIS assays were carried out with a potentiostat/galvanostat (Metrohm μ Autolab III) equipped with a frequency response analyzer module (FRA2). Measurements were performed at the applied voltage range from 0 to 4 V and fitted with the Nova software using the circuit model shown in Figure S9, Supporting Information. The AC signal amplitude was set to 10 mV and modulated in a frequency range from 10 to 1 MHz. The Nova 1.11 software was used to obtain the parameters from the equivalent circuit. With this data at hand, the resistance of the intrinsic non-doped region (R_{LEC}) was directly obtained. The film conductivity ($S\ m^{-1}$) is measured at 0 V with the following equation: $\sigma = d/(A \times R_{LEC})$, where d is the thickness of the layer, A is the area of the electrodes, and R_{LEC} is the resistance of the active layer. The dielectric constant ϵ_r was calculated with the formula $\epsilon_r = C \times L/(\epsilon_0 \times A)$, where C is the effective capacitance, L is the thickness of the active layer, ϵ_0 is the vacuum permittivity (8.85×10^{-12} F m^{-1}), and A is the active area of the device (10 mm^2).

[CCDC 2232405 contains the supplementary crystallographic data for this paper. These data can be obtained free of charge from The Cambridge Crystallographic Data Centre via www.ccdc.cam.ac.uk/data_request/cif.]

[Further details of the crystal structure investigation(s) may be obtained from Dr. Alexander Pöthig, TUM School of Natural Sciences, Department of Chemistry & Catalysis Research Center (CRC), Technical University of Munich, Lichtenbergstr. 4, 85 747 Garching (Germany), on quoting the depository number CSD-2232405]

Supporting Information

Supporting Information is available from the Wiley Online Library or from the author.

Acknowledgements

S.L. and L.M.C. contributed equally. R.D.C. acknowledges the European Union's Horizon 2020 research and innovation MSCA-ITN STiBNite No. 956923.

Open access funding enabled and organized by Projekt DEAL.

Conflict of Interest

The authors declare no conflict of interest.

Data Availability Statement

The data that support the findings of this study are available from the corresponding author upon reasonable request.

Keywords

dual-phosphorescence, red-emitting materials, silver nanoclusters, silver(I) complexes, stable light-emitting electrochemical cells

Received: December 30, 2022

Revised: February 15, 2023

Published online: May 13, 2023

- [1] R. D. Costa, *Light-Emitting Electrochemical Cells*, Springer, Cham 2017.
- [2] E. Fresta, R. D. Costa, *J. Mater. Chem. C* **2017**, *5*, 5643.
- [3] E. Fresta, R. D. Costa, *Adv. Funct. Mater.* **2020**, *30*, 1908176.
- [4] S. Tang, L. Edman, *Top. Curr. Mater.* **2016**, *374*, 40.
- [5] H.-C. Su, Y.-R. Chen, K.-T. Wong, *Adv. Funct. Mater.* **2020**, *30*, 1906898.
- [6] a) E. M. Lindh, A. Sandström, L. Edman, *Small* **2014**, *10*, 4148; b) A. Sandström, A. Asadpoordarvish, J. Enevold, L. Edman, *Adv. Mater.* **2014**, *26*, 4975; c) M. Pietsch, N. Casado, D. Mecerreyes, G. Hernandez-Sosa, *ACS Appl. Mater. Interfaces* **2022**, *14*, 43568; d) M. Pietsch, T. Rödlmeier, S. Schlisske, J. Zimmermann, C. Romero-Nieto, G. Hernandez-Sosa, *J. Mater. Chem. C* **2019**, *7*, 7121.
- [7] K. Matsuki, J. Pu, T. Takenobu, *Adv. Funct. Mater.* **2020**, *30*, 1908641.
- [8] a) K. Schlingman, Y. Chen, R. S. Carmichael, T. B. Carmichael, *Adv. Mater.* **2021**, *33*, 2006863; b) E. M. Lindh, A. Sandström, M. R. Andersson, L. Edman, *Light: Sci. Appl.* **2016**, *5*, 16050; c) A. Asadpoordarvish, A. Sandström, C. Larsen, R. Bollström, M. Toivakka, R. Österbacka, L. Edman, *Adv. Funct. Mater.* **2015**, *25*, 3238.
- [9] a) M. H. Bowler, A. Mishra, A. C. Adams, C. L.-D. Blangy, J. D. Slinker, *Adv. Funct. Mater.* **2020**, *30*, 1906715; b) J. Mindemark, L. Edman, *J. Mater. Chem. C* **2016**, *4*, 420; c) L. M. Cavinato, G. Millán, J. Fernández-Cestau, E. Fresta, E. Lalinde, J. R. Berenguer, R. D. Costa, *Adv. Funct. Mater.* **2022**, *32*, 2201975.
- [10] S. van Reenen, P. Matyba, A. Dzwilewski, R. A. J. Janssen, L. Edman, M. Kemerink, *J. Am. Chem. Soc.* **2010**, *132*, 13776.
- [11] S. Tang, A. Sandström, P. Lundberg, T. Lanz, C. Larsen, S. van Reenen, M. Kemerink, L. Edman, *Nat. Commun.* **2017**, *8*, 1190.
- [12] S. Tang, A. Sandström, P. Lundberg, T. Lanz, C. Larsen, S. van Reenen, M. Kemerink, L. Edman, *Nat. Commun.* **2017**, *8*, 1190.
- [13] G. U. Mahoro, J. Fernandez-Cestau, J.-L. Renaud, P. B. Coto, R. D. Costa, S. Gaillard, *Adv. Opt. Mater.* **2020**, *8*, 2000260.
- [14] C. E. Housecroft, E. C. Constable, *J. Mater. Chem. C* **2022**, *10*, 4456.
- [15] a) K. Youssef, Y. Li, S. O'Keeffe, L. Li, Q. Pei, *Adv. Funct. Mater.* **2020**, *30*, 1909102; b) K. Youssef, Y. Li, S. O'Keeffe, L. Li, Q. Pei, *Adv. Funct. Mater.* **2020**, *30*, 2070220.
- [16] E. Nannen, J. Frohleiks, S. Gellner, *Adv. Funct. Mater.* **2020**, *30*, 1907349.
- [17] S. Kanagaraj, A. Puthanveedu, Y. Choe, *Adv. Funct. Mater.* **2020**, *30*, 1907126.
- [18] a) S. Tang, H. A. Buchholz, L. Edman, *ACS Appl. Mater. Interfaces* **2015**, *7*, 25955; b) P. Lundberg, Q. Wei, Z. Ge, B. Voit, S. Reineke, L. Edman, *J. Phys. Chem. Lett.* **2020**, *11*, 6227.
- [19] a) J. C. John, K. Shanmugasundaram, C. V. S. Brahmmananda Rao, G. Gopakumar, Y. Choe, *J. Phys. Chem. C* **2021**, *125*, 17993; b) J. C. John, K. Shanmugasundaram, G. Gopakumar, Y. Choe, *ACS Photonics* **2022**, *9*, 203; c) M. D. Weber, M. Adam, R. R. Tykwinski, R. D. Costa, *Adv. Funct. Mater.* **2015**, *25*, 5066; d) E. Fresta, J. Dossó, J. Cabanillas-González, D. Bonifazi, R. D. Costa, *Adv. Funct. Mater.* **2020**, *30*, 1906830; e) S. Tang, P. Lundberg, Y. Tsuchiya, J. Ràfols-Ribé, Y. Liu, J. Wang, C. Adachi, L. Edman, *Adv. Funct. Mater.* **2022**, *32*, 2205967; f) P. Lundberg, Y. Tsuchiya, E. M. Lindh, S. Tang, C. Adachi, L. Edman, *Nat. Commun.* **2019**, *10*, 5307.
- [20] a) S. Park, J. Yang, S. Kim, D. Hahm, H. Jo, W. K. Bae, M. S. Kang, *Adv. Opt. Mater.* **2020**, *8*, 2001535; b) J. Frohleiks, S. Wepfer, Y. Kelestemur, H. V. Demir, G. Bacher, E. Nannen, *ACS Appl. Mater. Interfaces* **2016**, *8*, 24692; c) J. Frohleiks, S. Gellner, S. Wepfer, G. Bacher, E. Nannen, *ACS Appl. Mater. Interfaces* **2018**, *10*, 42637; d) Y. Liu, S. Tang, X. Wu, N. Boulanger, E. Gracia-Espino, T. Wågberg, L. Edman, J. Wang, *Nano*

- Res. **2022**, 15, 5610; e) Y.-H. Tang, Y.-C. Chiu, D. Luo, J.-Y. Lien, R.-H. Yi, C.-H. Lin, Z.-P. Yang, C.-W. Lu, H.-C. Su, *Chem. Eur. J.* **2020**, 26, 13668.
- [21] a) M. F. Aygüler, B. M. D. Puscher, Y. Tong, T. Bein, A. S. Urban, R. D. Costa, P. Docampo, *J. Phys. D: Appl. Phys.* **2018**, 51, 334001; b) M. F. Aygüler, M. D. Weber, B. M. D. Puscher, D. D. Medina, P. Docampo, R. D. Costa, *J. Phys. Chem. C* **2015**, 119, 12047; c) A. Mishra, M. Alahbakhshi, R. Haroldson, L. D. Bastatas, Q. Gu, A. A. Zakhidov, J. D. Slinker, *Adv. Opt. Mater.* **2020**, 8, 2000226; d) A. Mishra, M. Alahbakhshi, R. Haroldson, Q. Gu, A. A. Zakhidov, J. D. Slinker, *Adv. Funct. Mater.* **2021**, 31, 2102006; e) A. Mishra, R. Bose, Y. Zheng, W. Xu, R. McMullen, A. B. Mehta, M. J. Kim, J. W. P. Hsu, A. V. Malko, J. D. Slinker, *Adv. Mater.* **2022**, 34, 2203226; f) D. Gets, M. Alahbakhshi, A. Mishra, R. Haroldson, A. Papadimitratos, A. Ishteev, D. Saranin, S. Anoshkin, A. Pushkarev, E. Danilovskiy, S. Makarov, J. D. Slinker, A. A. Zakhidov, *Adv. Opt. Mater.* **2021**, 9, 2001715; g) W.-L. Kang, Y.-T. Tsai, Y.-C. Ji, R.-H. Yi, Y.-X. Wang, H.-L. Shen, X.-J. Chen, Y.-C. Hsu, C.-W. Lu, Z.-P. Yang, H. C. Su, *Chem. Eur. J.* **2021**, 27, 17785.
- [22] L. M. Cavinato, S. Wölfl, A. Pöthig, E. Fresta, C. Garino, J. Fernandez-Cestau, C. Barolo, R. D. Costa, *Adv. Mater.* **2022**, 34, 2109228.
- [23] a) C. D. Ertl, C. Momblona, A. Pertegás, J. M. Junquera-Hernández, M.-G. La-Placa, A. Prescimone, E. Ortí, C. E. Housecroft, E. C. Constable, H. J. Bolink, *J. Am. Chem. Soc.* **2017**, 139, 3237; b) H. J. Bolink, E. Coronado, R. D. Costa, E. Ortí, M. Sessolo, S. Graber, K. Doyle, M. Neuburger, C. E. Housecroft, E. C. Constable, *Adv. Mater.* **2008**, 20, 3910.
- [24] J. Gao, *ChemPlusChem* **2018**, 83, 183.
- [25] D. Tordera, S. Meier, M. Lenes, R. D. Costa, E. Ortí, W. Sarfert, H. J. Bolink, *Adv. Mater.* **2012**, 24, 897.
- [26] a) R. Bai, X. Meng, X. Wang, L. He, *Adv. Funct. Mater.* **2020**, 30, 1907169; b) C. Zhang, R. Liu, D. Zhang, L. Duan, *Adv. Funct. Mater.* **2020**, 30, 1907156.
- [27] J. Emsley, *Nature's Building Blocks: An A-Z Guide to the Elements*, Oxford University Press, Oxford **2011**.
- [28] S. Keller, A. Pertegás, G. Longo, L. Martínez, J. Cerdá, J. M. Junquera-Hernández, A. Prescimone, E. C. Constable, C. E. Housecroft, E. Ortí, H. J. Bolink, *J. Mater. Chem. C* **2016**, 4, 3872.
- [29] S. Keller, A. Prescimone, H. Bolink, M. Sessolo, G. Longo, L. Martínez-Sarti, J. M. Junquera-Hernández, E. C. Constable, E. Ortí, C. E. Housecroft, *Dalton Trans.* **2018**, 47, 14263.
- [30] S. Keller, E. C. Constable, C. E. Housecroft, M. Neuburger, A. Prescimone, G. Longo, A. Pertegás, M. Sessolo, H. J. Bolink, *Dalton Trans.* **2014**, 43, 16593.
- [31] G. U. Mahoro, E. Fresta, M. Elie, D. Di Nasso, Q. Zhang, J.-F. Lohier, J.-L. Renaud, M. Linares, R. Wannemacher, J. Cabanillas-Gonzalez, R. D. Costa, S. Gaillard, *Dalton Trans.* **2021**, 50, 11049.
- [32] M. D. Weber, E. Fresta, M. Elie, M. E. Miehllich, J.-L. Renaud, K. Meyer, S. Gaillard, R. D. Costa, *Adv. Funct. Mater.* **2018**, 28, 1707423.
- [33] B. Pashaei, S. Karimi, H. Shahroosvand, P. Abbasi, M. Pilkington, A. Bartolotta, E. Fresta, J. Fernandez-Cestau, R. D. Costa, F. Bonaccorso, *Chem. Soc. Rev.* **2019**, 48, 5033.
- [34] E. Fresta, G. U. Mahoro, L. M. Cavinato, J.-F. Lohier, J.-L. Renaud, S. Gaillard, R. D. Costa, *Adv. Opt. Mater.* **2022**, 10, 2101999.
- [35] E. Fresta, M. D. Weber, J. Fernandez-Cestau, R. D. Costa, *Adv. Opt. Mater.* **2019**, 7, 1900830.
- [36] M. D. Weber, J. E. Wittmann, A. Burger, O. B. Malcioğlu, J. Segarra-Martí, A. Hirsch, P. B. Coto, M. Bockstedte, R. D. Costa, *Adv. Funct. Mater.* **2016**, 26, 6737.
- [37] a) M. Iwamura, S. Takeuchi, T. Tahara, *Acc. Chem. Res.* **2015**, 48, 782; b) M. D. Weber, C. Garino, G. Volpi, E. Casamassa, M. Milanesio, C. Barolo, R. D. Costa, *Dalton Trans.* **2016**, 45, 8984; c) C. T. Cunningham, J. J. Moore, K. L. Cunningham, P. E. Fanwick, D. R. McMillin, *Inorg. Chem.* **2000**, 39, 3638; d) L. X. Chen, G. Jennings, T. Liu, D. J. Gosztola, J. P. Hessler, D. V. Scaltrito, G. J. Meyer, *J. Am. Chem. Soc.* **2002**, 124, 10861; e) M. W. Mara, K. A. Fransted, L. X. Chen, *Coord. Chem. Rev.* **2015**, 282, 2.
- [38] O. Moudam, A. C. Tsipis, S. Kommanaboyina, P. N. Horton, S. J. Coles, *RSC Adv.* **2015**, 5, 95047.
- [39] a) A. Kaeser, O. Moudam, G. Accorsi, I. Séguy, J. Navarro, A. Belbakra, C. Duhayon, N. Armaroli, B. Delavaux-Nicot, J.-F. Nierengarten, *Eur. J. Inorg. Chem.* **2014**, 2014, 1345; b) M. Z. Shafikov, A. F. Suleymanova, R. Czerwieniec, H. Yersin, *Chem. Mater.* **2017**, 29, 1708; c) M. Z. Shafikov, A. F. Suleymanova, A. Schinabeck, H. Yersin, *J. Phys. Chem.* **2018**, 9, 702; d) D. Zare, C. Pigué, A. Prescimone, C. E. Housecroft, E. C. Constable, *Chem. Eur. J.* **2022**, 28, 202200912.
- [40] J. M. Carbonell-Vilar, E. Fresta, D. Armentano, R. D. Costa, M. Viciano-Chumillas, J. Cano, *Dalton Trans.* **2019**, 48, 9765.
- [41] E. Fresta, J. M. Carbonell-Vilar, J. Yu, D. Armentano, J. Cano, M. Viciano-Chumillas, R. D. Costa, *Adv. Funct. Mater.* **2019**, 29, 1901797.
- [42] A. V. Artem'ev, M. Z. Shafikov, A. Schinabeck, O. V. Antonova, A. S. Berezin, I. Y. Bagryanskaya, P. E. Plusnin, H. Yersin, *Inorg. Chem. Front.* **2019**, 6, 3168.
- [43] M. Z. Shafikov, R. Czerwieniec, H. Yersin, *Dalton Trans.* **2019**, 48, 2802.
- [44] T. Teng, K. Li, G. Cheng, Y. Wang, J. Wang, J. Li, C. Zhou, H. Liu, T. Zou, J. Xiong, C. Wu, H.-X. Zhang, C.-M. Che, C. Yang, *Inorg. Chem.* **2020**, 59, 12122.
- [45] M. Calvo, O. Crespo, M. C. Gimeno, A. Laguna, M. T. Oliván, V. Polo, D. Rodríguez, J.-M. Sáez-Rocher, *Inorg. Chem.* **2020**, 59, 14447.
- [46] J.-H. Jia, D. Liang, R. Yu, X.-L. Chen, L. Meng, J.-F. Chang, J.-Z. Liao, M. Yang, X.-N. Li, C.-Z. Lu, *Chem. Mater.* **2020**, 32, 620.
- [47] C.-W. Hsu, C.-C. Lin, M.-W. Chung, Y. Chi, G.-H. Lee, P.-T. Chou, C.-H. Chang, P.-Y. Chen, *J. Am. Chem. Soc.* **2011**, 133, 12085.
- [48] B. Nemati Bideh, H. Shahroosvand, M. K. Nazeeruddin, *Inorg. Chem.* **2021**, 60, 11915.
- [49] M. Beliaeva, A. Belyaev, E. V. Grachova, A. Steffen, I. O. Koshevoy, *J. Am. Chem. Soc.* **2021**, 143, 15045.
- [50] E. Fresta, G. Volpi, M. Milanesio, C. Garino, C. Barolo, R. D. Costa, *Inorg. Chem.* **2018**, 57, 10469.
- [51] a) C. Hansch, A. Leo, R. W. Taft, *Chem. Rev.* **1991**, 91, 165; b) H. C. Brown, Y. Okamoto, *J. Am. Chem. Soc.* **1958**, 80, 4979; c) D. H. McDaniel, H. C. Brown, *J. Org. Chem.* **1958**, 23, 420.
- [52] S. Keller, A. Pertegás, G. Longo, L. Martínez, J. Cerdá, J. M. Junquera-Hernández, A. Prescimone, E. C. Constable, C. E. Housecroft, E. Ortí, H. J. Bolink, *J. Mater. Chem. C* **2016**, 4, 3857.
- [53] a) A. Kaeser, M. Mohankumar, J. Mohanraj, F. Monti, M. Holler, J.-J. Cid, O. Moudam, I. Nierengarten, L. Karmazin-Brelot, C. Duhayon, B. Delavaux-Nicot, N. Armaroli, J.-F. Nierengarten, *Inorg. Chem.* **2013**, 52, 12140; b) E. Leoni, J. Mohanraj, M. Holler, M. Mohankumar, I. Nierengarten, F. Monti, A. Sournia-Saquet, B. Delavaux-Nicot, I. N. Jean-Franco, N. Armaroli, *Inorg. Chem.* **2018**, 57, 15537; c) M. Mohankumar, M. Holler, J.-F. Nierengarten, J.-P. Sauvage, *Chem. Eur. J.* **2012**, 18, 12192; d) T.-A. Phan, N. Armaroli, A. Saavedra Moncada, E. Bandini, B. Delavaux-Nicot, J.-F. Nierengarten, D. Armspach, *Angew. Chem. Int. Ed.* **2022**, 62, 202214638; e) B. Ralahy, U. Hahn, E. Wasielewski, J.-F. Nierengarten, *Eur. J. Inorg. Chem.* **2021**, 26, 2625.
- [54] M. Meyer, F. Brunner, A. Prescimone, E. C. Constable, C. E. Housecroft, *Molecules* **2020**, 26, 125.
- [55] S. Igawa, M. Hashimoto, I. Kawata, M. Hoshino, M. Osawa, *Inorg. Chem.* **2012**, 51, 5805.
- [56] P. G. Hoertz, A. Staniszewski, A. Marton, G. T. Higgins, C. D. Incavito, A. L. Rheingold, G. J. Meyer, *J. Am. Chem. Soc.* **2006**, 128, 8234.
- [57] L. Yang, D. R. Powell, R. P. Houser, *Dalton Trans.* **2007**, 9, 955.
- [58] P. Dierkes, P. W. N. M. van Leeuwen, *J. Chem. Soc., Dalton Trans.* **1999**, 10, 1519.
- [59] P. Mulvaney, A. Henglein, *J. Phys. Chem.* **1990**, 94, 4182.
- [60] a) E. Fresta, J. Dosso, J. Cabanillas-Gonzalez, D. Bonifazi, R. D. Costa, *ACS Appl. Mater. Interfaces* **2020**, 12, 28426; b) J. Ràfols-Ribé, N. D.

- Robinson, C. Larsen, S. Tang, M. Top, A. Sandström, L. Edman, *Adv. Funct. Mater.* **2020**, *30*, 1908649.
- [61] a) J.-M. Saveant, *Elements of Molecular and Biomolecular Electrochemistry*, John Wiley & Sons, Hoboken, NJ **2006**; b) N. Elgrishi, K. J. Rountree, B. D. McCarthy, E. S. Rountree, T. T. Eisenhart, J. L. Dempsey, *J. Chem. Educ.* **2018**, *95*, 197.
- [62] a) S. K. Emashova, A. A. Titov, O. A. Filippov, A. F. Smol'yakov, E. M. Titova, L. M. Epstein, E. S. Shubina, *Eur. J. Inorg. Chem.* **2019**, *2019*, 4855; b) M.-Y. Leung, M.-C. Tang, W.-L. Cheung, S.-L. Lai, M. Ng, M.-Y. Chan, V. Wing-Wah Yam, *J. Am. Chem. Soc.* **2020**, *142*, 2448; c) J. Li, L. Wang, Z. Zhao, X. Li, X. Yu, P. Huo, Q. Jin, Z. Liu, Z. Bian, C. Huang, *Angew. Chem. Int. Ed.* **2020**, *59*, 8210; d) S. Nayeri, S. Jamali, A. Jamjah, J. R. Shakirova, S. P. Tunik, V. Gurzhiy, H. Samouei, H. R. Shahsavari, *Inorg. Chem.* **2020**, *59*, 5702; e) M.-C. Tang, M.-Y. Leung, S.-L. Lai, M. Ng, M.-Y. Chan, V. Wing-Wah Yam, *J. Am. Chem. Soc.* **2018**, *140*, 13115.
- [63] a) Y. Liu, M. S. Liu, A.-Y. Jen, *Acta Polym.* **1999**, *50*, 105; b) S.-W. Hwang, Y. Chen, *Macromolecules* **2002**, *35*, 5438; c) L. F. C. Nart, I. A. Hümmelgen, *J. Solid State Electrochem.* **2002**, *7*, 55.
- [64] L. D. Bastatas, M. D. Moore, J. D. Slinker, *ChemPlusChem* **2018**, *83*, 266.
- [65] L. D. Bastatas, K.-Y. Lin, M. D. Moore, K. J. Suhr, M. H. Bowler, Y. Shen, B. J. Holliday, J. D. Slinker, *Langmuir* **2016**, *32*, 9468.
- [66] a) B. M. D. Puscher, M. F. Aygüler, P. Docampo, R. D. Costa, *Adv. Energy Mater.* **2017**, *7*, 1602283; b) S. B. Meier, D. Hartmann, A. Winacker, W. Sarfert, *J. Appl. Phys.* **2014**, *116*, 104504; c) A. Munar, A. Sandström, S. Tang, L. Edman, *Adv. Funct. Mater.* **2012**, *22*, 1511.
- [67] a) K. J. Suhr, L. D. Bastatas, Y. Shen, L. A. Mitchell, B. J. Holliday, J. D. Slinker, *ACS Appl. Mater. Interfaces* **2016**, *8*, 8888; b) K.-Y. Lin, L. D. Bastatas, K. J. Suhr, M. D. Moore, B. J. Holliday, M. Minary-Jolandan, J. D. Slinker, *ACS Appl. Mater. Interfaces* **2016**, *8*, 16776.
- [68] E. Engel, R. M. Dreizler, *Density Functional Theory: An Advanced Course*, Springer, Heidelberg **2011**.
- [69] a) Y. Zhao, N. E. Schultz, D. G. Truhlar, *J. Chem. Phys.* **2005**, *123*, 161103; b) Y. Zhao, D. G. Truhlar, *Theor. Chem. Acc* **2008**, *120*, 215.
- [70] F. Weigend, R. Ahlrichs, *Phys. Chem. Chem. Phys.* **2005**, *7*, 3297.
- [71] D. Andrae, U. Huermann, M. Dolg, H. Stoll, H. Preu, *Theor. Chim. Acta* **1990**, *77*, 123.
- [72] C. Ullrich, *Time-Dependent Density-Functional Theory: Concepts and Applications*, Oxford University Press, Oxford **2012**.
- [73] a) J. Andzelm, C. Kölmel, A. Klamt, *J. Chem. Phys.* **1995**, *103*, 9312; b) V. Barone, M. Cossi, *J. Phys. Chem. A* **1998**, *102*, 1995; c) M. Cossi, N. Rega, G. Scalmani, V. Barone, *J. Comput. Chem.* **2003**, *24*, 669; d) A. Klamt, G. Schüürmann, *J. Chem. Soc., Perkin Trans. 2* **1993**, *2*, 799.
- [74] R. L. Martin, *J. Chem. Phys.* **2003**, *118*, 4775.
- [75] M. J. Frisch, G. W. Trucks, H. B. Schlegel, G. E. Scuseria, M. A. Robb, J. R. Cheeseman, G. Scalmani, V. Barone, G. A. Petersson, H. Nakatsuji, X. Li, M. Caricato, A. V. Marenich, J. Bloino, B. G. Janesko, R. Gomperts, B. Mennucci, H. P. Hratchian, J. V. Ortiz, A. F. Izmaylov, J. L. Sonnenberg, D. Williams-Young, F. Ding, F. Lipparini, F. Egidi, J. Goings, B. Peng, A. Petrone, T. Henderson, D. Ranasinghe, et al., *Gaussian 16, Revision A.03*, Gaussian, Inc., Wallingford, CT **2016**.
- [76] a) E. van Lenthe, E. J. Baerends, J. G. Snijders, *J. Chem. Phys.* **1993**, *99*, 4597; b) E. van Lenthe, E. J. Baerends, J. G. Snijders, *J. Chem. Phys.* **1994**, *101*, 9783.
- [77] J. D. Rolfes, F. Neese, D. A. Pantazis, *J. Comput. Chem.* **2020**, *41*, 1842.
- [78] a) F. Neese, F. Wennmohs, U. Becker, C. Riplinger, *J. Appl. Phys.* **2020**, *152*, 224108; b) K. E. Riley, P. Hobza, *Wiley Interdiscip. Rev.: Comput. Mol. Sci.* **2011**, *1*, 3; c) F. Weigend, *Phys. Chem. Chem. Phys.* **2006**, *8*, 1057.
- [79] F. Neese, *J. Chem. Phys.* **2005**, *122*, 034107.
- [80] a) G. Sheldrick, *SHELXL-2014/7: Program for the Solution of Crystal Structures*, University of Göttingen, Göttingen, Germany **2014**; b) G. Sheldrick, *SHELXL-97 (Release 97-2)*, University of Göttingen Journal, **1998**.
- [81] C. B. Hübschle, G. M. Sheldrick, B. Dittrich, *J. Appl. Crystallogr.* **2011**, *44*, 1281.
- [82] A. Wilson, in *International Tables for Crystallography, Volume C: Mathematical, Physical and Chemical Tables* (Ed: E. Prince), Kluwer, Dordrecht, The Netherlands **1992**, pp. 500–502, 219–222, 193–199.